PAPER

Check for updates

Fe-doped CuCo$_2$S$_4$ thiospinel as a high-performance oxygen electrocatalyst for rechargeable all-solid-state zinc–air batteries

Ravinder Sharma,[c] Abhay Rawat,[a] Arkaj Singh,[c] Jinta Merlin johny,[b] Akriti Gautam,[c] Jayanta Parui,[b] Tisita Das [ID][a] and Aditi Halder [ID] *[c]

The commercial viability of rechargeable zinc–air batteries (ZABs) is hindered by their poor round-trip efficiency, the dendritic growth of the anode and expensive cathode electrocatalysts with limited stability and durability in alkaline media during prolonged operation. Thus, exploratory research studies are essential to replace these platinum-group noble metal catalysts with other stable transition metal oxides. In this work, we demonstrate the facile one-step hydrothermal synthesis of Fe-doped CuCo$_2$S$_4$ thiospinels. Both experimental and theoretical analyses confirm that Fe incorporation into the CuCo$_2$S$_4$ lattice markedly enhances its electrocatalytic activity for the ORR and OER compared with the undoped material by modulating the electronic structure and elevating the metal valence states. The optimized composition, Fe$_{0.03}$CuCo$_2$S$_4$, exhibits outstanding bifunctional activity with an oxygen reduction reaction (ORR) onset potential of 0.89 V *vs.* RHE, a half-wave potential ($E_{1/2}$) of 0.80 V *vs.* RHE, and an oxygen evolution reaction (OER) overpotential of 330 mV at 10 mA cm^{-2}, resulting in a low bifunctional voltage gap (ΔE) of 0.76 V. Furthermore, a prototype ZAB assembled using Fe$_{0.03}$CCS as the air cathode delivers a peak power density of 82 mW cm^{-2} and a specific capacity of 803.4 mA h g$_{Zn}^{-1}$. The battery demonstrates excellent cycling stability, maintaining performance over 200 cycles (75 hours) at 5 mA cm^{-2} with 20 minutes charge–discharge intervals. During the depth of discharge study for extended charge–discharge durations (up to 6 hours cycles), the ZAB retains impressive stability for over 50 hours. This study highlights a promising strategy for designing efficient bifunctional electrocatalysts, paving the way for practical applications in next-generation zinc–air batteries.

Introduction

Fossil fuel-based energy systems are largely responsible for the economic expansion and modernization of growing economies.[1] However, the declining fossil fuel reserves, coupled with the rising global energy demand, pose a serious threat to the long-term sustainability of the global energy supply.[2] To foster a sustainable energy ecosystem, it is important to utilize renewable energy resources.[3] Unfortunately, the intermittent nature of renewable energy makes it vulnerable during practical applications.[4] Hence, to ensure the uninterrupted use of renewable energy, it is important to store it using energy storage devices. This allows users the flexibility and keeps a balance between the supply and demand chains, not restricted by the period of abundance. Therefore, the development of alternative electrochemical energy storage systems (like Zn–air batteries) and conversion systems (*e.g.* fuel cells) will build a sustainable ecosystem to address the energy crisis of the 21st century for sustainable and clean energy technology.[5–7]

Among many kinds of metal–air batteries, the zinc–air battery has attracted serious attention due to its low cost, environmental friendliness and high theoretical energy density (1086 Wh kg^{-1}).[8–10] The operating voltage of the zinc–air battery is around 1.65 V,[11] which is not a very high voltage for degrading the electrolyte in the aqueous medium. In terms of cost comparison, Li ion batteries cost between $200 and $250 per kWh, whereas zinc–air batteries cost only $150 per kWh. An efficient rechargeable zinc–air battery requires a bifunctional electrode material, which could efficiently perform the oxygen reduction reaction (ORR) during discharging and the oxygen evolution reaction (OER) during charging.[12–14] Unfortunately, both these processes involve multielectron and multistep transfer processes, making the reaction kinetics sluggish.[15–17] The sluggish kinetics for OER and ORR increase the voltage gap between charging and discharging cycles, which leads to a low round-trip efficiency of zinc air battery in a range from 55 to

[a]Materials Theory for Energy Scavenging (MATES) Lab, Department of Physics, Harish-Chandra Research Institute (HRI), A CI of Homi Bhabha National Institute (HBNI), Chhatnag Road, Jhunsi, Prayagraj 211019, India

[b]Chemistry Division, School of Advanced Sciences, VIT University, Chennai Campus, Chennai, 600127, India

[c]School of Chemical Sciences, Indian Institute of Technology Mandi, Himachal Pradesh 175005, India. E-mail: aditi@iitmandi.ac.in

2218 | *J. Mater. Chem. A*, 2026, **14**, 2218–2234

This journal is © The Royal Society of Chemistry 2026

65%.[18] To lower the cost of the battery and to maintain a stable energy supply, it is important to develop and design an improved cathode material with good bifunctional activity.

There are many strategies adopted by different research groups to improve the bifunctional activity of the electrode in the rechargeable ZAB.[19–21] Two well-adapted strategies to improve the reversible capacity and electrochemical energy storage in batteries is surface structure engineering and interlayer spacing expansion.[22] Heteroatom insertion in the crystal lattice is found to be effective in regulating the physicochemical properties of the electrode materials at the atomic level.[23,24] Recently, ternary thiospinel (AB_2S_4)[25,26] materials have gained more attention as oxygen bifunctional electrocatalysts. Thiospinels have two metal ions (A^{2+} and B^{3+}) occupying a tetrahedral site and an octahedral position with a sulfur atom in a closely packed crystal structure, respectively.[27] Such a structure with many redox centers can facilitate low-energy electron hopping between various metal cations, improving electrical conductivity and providing a large number of active sites for oxygen species adsorption and desorption.[28]

In this work, we explore a spinel chalcogenide ($CuCo_2S_4$) as a bifunctional cathode material for zinc–air batteries. We systematically introduce Fe as a dopant into the spinel lattice without disrupting its original crystal structure. The atomic radii of Fe and Co are very similar (125 pm and 126 pm, respectively), and their comparable size facilitates the substitution of Co^{3+} with Fe^{3+} within the $CuCo_2S_4$ framework (Fig. 1). This incorporation leads to a slight lattice expansion and improves the electrochemical reaction kinetics by optimizing the electronic structure and active-site configuration. Lattice strain, both compressive and tensile, can tune the intermediate binding strength and modulate the electronic configuration of transition metal cations, which consequently enhances the catalytic activity. A similar observation is also noted here. The undoped $CuCo_2S_4$ shows excellent bifunctional activity with a half-wave potential of 0.76 V for the ORR and an overpotential of 370 mV at 10 mA cm^{-2} for the OER, leading to a bifunctional activity (ΔE) of 0.84 V, which is capable of producing a power density of 52 mW cm^{-2} and a specific capacity of 748.8 mA h g$_{Zn}^{-1}$. The systematic doping of Fe in $CuCo_2S_4$ improves the bifunctional activity, achieving a positive half-wave potential of 0.80 V for the ORR and an overpotential of 330 mV at 10 mA cm^{-2} for the OER, leading to a bifunctional activity of 0.76 V, which leads to the maximum power density of 82 mW cm^{-2}

and a specific capacity of 803.4 mA h g$_{Zn}^{-1}$. The maximum round-trip efficiency is found to be 61.72%. The optimization of the dopant Fe in the spinel chalcogenide is crucial. Our experimental data show that excessive Fe doping leads to the failure of the performance and phase segregation. Thus, the systematic and calculated doping of Fe in $CuCo_2S_4$ is important to improve its battery performance and rechargeability. Theoretical DFT calculations also reveal that the overpotential values decrease significantly on the doped surface, and the Co site is the best possible active site with the lowest overpotential among all the considered active sites. Substitutional doping modifies the local electronic structure and directly influences the electron transfer between the surface and adsorbates, thereby facilitating the OER process and improving the bifunctional activity.

Experimental section

Chemicals and materials

Cobalt(II) acetate tetrahydrate [Co(CH$_3$COO)$_2$·4H$_2$O, 99%] and ethylene diamine (EDA) (99.5%) were purchased from SRL Chemicals. Cupric acetate monohydrate [Cu(CH$_3$COO)$_2$·H$_2$O, 99.0%], a pure sulphur powder and KOH were purchased from Loba Chemicals. Iron(III) chloride hexahydrate [FeCl$_3$·6H$_2$O] was purchased from Himedia, while Pt/C and RuO$_2$ were purchased from Alfa Aesar and Sigma Aldrich, respectively. A Nafion 5 wt% solution was purchased from Metnmat Innovations. All chemicals were used without further purification.

Synthesis of pure copper cobalt sulfide (CCS)

Briefly, to synthesize copper cobalt sulfide (CCS), 1 mmol of copper acetate (0.1996 g) and 2 mmol of cobalt acetate (0.4982 g) were dissolved in 30 mL of deionized water under vigorous stirring for 10 minutes to form a homogeneous solution. In a separate beaker, an S-EDA complex was prepared by adding 4 mmol of sulphur powder to 3 mL of ethylene diamine. The deep-red complex was then added dropwise to the homogeneous solution of copper acetate and cobalt acetate with constant stirring to form a dark-brown solution. The dark-brown solution was transferred to a Teflon-lined hydrothermal autoclave and heated to 180 °C for 12 h in an oven. After 12 h, the hydrothermal autoclave was allowed to cool naturally to room temperature, and the black precipitate was collected through centrifugation and washed several times with DI water and ethanol. The collected sample was dried in an oven at 50 °C. The synthesis scheme is given in Fig. 2(a).

Synthesis of Fe-doped samples Fe$_x$CCS

The Fe-doped samples were synthesized following the same procedure with varying amounts of FeCl$_3$·6H$_2$O added to the copper acetate and cobalt acetate precursor solution, followed by the dropwise addition of the S–EDA complex and subsequent hydrothermal reaction. The elemental composition of the Fe$_x$-CuCo$_2$S$_4$ samples was quantified using inductively coupled plasma mass spectrometry (ICP-MS). The obtained Fe, Cu, and Co ratios confirmed the successful incorporation of Fe into the CuCo$_2$S$_4$ (Table S1).
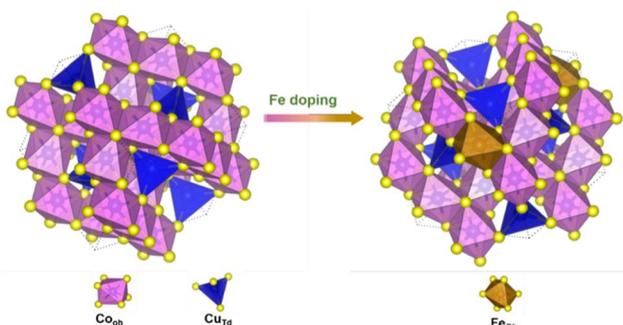

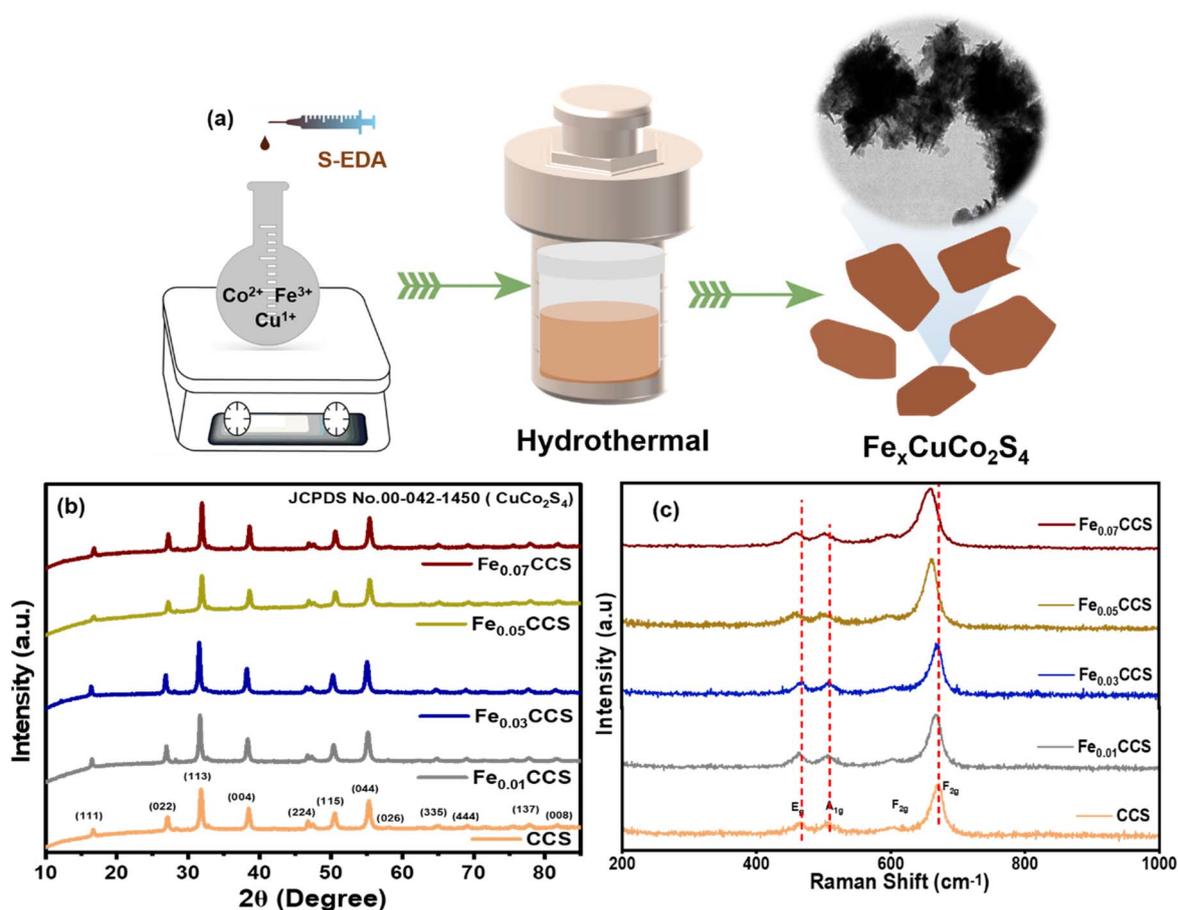**Fig. 1** Schematic of the crystal structure of Fe-doped samples Fe$_x$CCS.

This journal is © The Royal Society of Chemistry 2026

J. Mater. Chem. A, 2026, **14**, 2218–2234 | **2219**

Fig. 2 (a) Schematic of the synthesis of $Fe_xCuCo_2S_4$. (b) XRD patterns of $CuCo_2S_4$ and $Fe_xCuCo_2S_4$ (X = 0.01, 0.03, 0.05 and 0.07). (c) Raman spectra of $CuCo_2S_4$ and $Fe_xCuCo_2S_4$ (X = 0.01, 0.03, 0.05 and 0.07).

Physical characterisation

The crystal structure examination was done with the help of Rigaku MiniFlex. The diffractions were recorded in the 2θ range from $10°$ to $85°$ at a one-degree scan rate with Cu Kα radiation ($\lambda = 0.154$ nm). Raman spectra were recorded using LabRAM HR Evolution, Horiba Jobin Vyon, with a 532 nm laser. The morphological analysis of the catalyst was done using a field-emission scanning electron microscope (FE-SEM) facility (Nova Nano SEM 450). Further, high-resolution transmission electron microscopy (HRTEM) was performed using a Tecnai G2 20 S-TWIN TEM at an acceleration voltage of 200 kV employing LaB$_6$ as an electron source. The surface and chemical composition analyses of the catalyst were performed by X-ray photoelectron spectroscopy using Thermo Fisher Scientific Nexsa, employing Al-Kα ($\lambda = 1486.6$ eV). All the binding energies were calibrated with the C 1s peak at 284.8 eV.

Electrochemical characterisation

OER studies

All electrochemical studies were performed with a conventional three-electrode assembly in a single-compartment cell, wherein a glassy carbon electrode (GCE, $\varnothing = 5$ mm) containing the drop-coated catalyst acted as the working electrode (WE), a Pt wire acted as the counter electrode, and Ag/AgCl (3 M KCl) served as the reference electrode. The electrochemical measurement was done with the help of an electrochemical workstation (Autolab, Metrohm) using a N$_2$-purged 1 M KOH solution as the electrolyte. Before each analysis, the GCE was cleaned with an alumina slurry of different grits (1, 0.3 and 0.1 μm grain sizes, respectively) and washed with deionized water. Electrochemical impedance spectroscopy (EIS) measurements were performed in the frequency range from 1 MHz to 0.1 Hz. To prepare the working electrode for electrochemical measurements, 3 mg of the powder catalyst, mixed with 3 mg of Vulcan carbon, was dispersed in a blend of deionized water and isopropyl alcohol (2 : 1) containing 15 μL of the Nafion solution (5 wt%) as a binder, and it was ultrasonicated for 30–40 min to form a homogeneous catalyst ink. The loading of the catalyst ink on the GCE was kept at 99.6 μg cm^{-2}. All the potentials were referred to the RHE for convenience, and the current density was normalized by dividing the obtained current by the geometric area of the electrode.

ORR studies

To evaluate the ORR activity of the synthesized catalyst, hydrodynamic experiments, namely, rotating disk electrode (RDE)

2220 | J. Mater. Chem. A, 2026, 14, 2218–2234

This journal is © The Royal Society of Chemistry 2026

and rotating ring-disk electrode (RRDE) measurements, were performed in 0.1 M KOH. The experiments were performed at various rotation rates between 225 and 2025 rpm at a scan rate of 5 mV s^{-1} in a three-electrode assembly using a glassy carbon disk-Au ring (Ø = 5.5 mm) ring-disk electrode from Pine Research Instrument Inc., USA, as a WE with 10 μL (200 μg cm^{-2}) of the catalyst slurry drop-coated on the GCE disk. The measurements were performed under an inert atmosphere (purged with N$_2$) and in an oxygen (O$_2$)-saturated medium by bubbling it through the electrolyte for 30 min before the start of the experiment, and then, a constant flow was maintained above the electrolyte throughout the measurements.

Rechargeable aqueous zinc–air battery

For practical application, an aqueous rechargeable ZAB was assembled in a two-electrode setup. The cathode part was designed using a porous carbon paper (1 cm × 1 cm) coated with the catalyst ink as a support. The catalyst ink was prepared by dispersing 5 mg of the catalyst with 10 mg of Vulcan carbon in a mixture of IPA (485 μL) and DI water (485 μL) with the addition of 30 μL of the Nafion solution (5 wt%). Then, 150 μL of the catalyst ink was drop-casted over the carbon paper in a 1 cm × 1 cm area. A polished Zn foil with the same area was used as an anode. The electrolyte used for the aqueous ZAB testing was 6 M KOH with 0.2 M Zn(acetate)$_2$.

Rechargeable solid-state zinc–air battery

Further, Fe$_{0.03}$CCS catalysts were also used in solid-state zinc–air batteries to explore their wider applications. The cathode was made using a conductive carbon cloth as the substrate, and 200 μL of the ink containing the active catalyst was drop-casted over 1 sq. cm^2 area of the carbon cloth, resulting in a loading of 1 mg cm^{-2}. A PVA KOH membrane was used as the active solid-state electrolyte, which was prepared using 1.5 g of PVA in 12 mL of water at 80 °C till the solution became viscous. Then, 3 mL of 9 M KOH was added to the solution with constant stirring. Then, the solution was poured into a glass Petri dish for drying. After drying, the PVA KOH membrane was dipped in 6 M KOH for further saturation of the electrolyte in the membrane. Further, this membrane was sandwiched between the cathode and zinc anode to make the solid-state battery.

Results and discussion

Undoped CuCo$_2$S$_4$ is in the spinel phase with the space group of $Fd3m$. The thiospinel CuCo$_2$S$_4$, having the general formula AB$_2$S$_4$, is composed of trivalent Co^{3+} ions occupying octahedral B sites and divalent Cu^{2+} ions present at the tetrahedral A site. The crystalline structure of the synthesized catalyst was examined using the powder X-ray diffraction technique, which confirms the crystal structure. The XRD pattern of CCS shows the diffraction peaks at 16.69°, 27.11°, 31.78°, 38.46°, 46.76°, 50.50°, 55.28°, 64.91°, 69.12°, 77.85°, and 81.70°, which are

indexed to the (111), (022), (113), (004), (224), (115), (044), (335), (444), (137) and (008) planes, respectively (Fig. 2(b)). The XRD pattern of CCS well matches the carrollite structure of CuCo$_2$S$_4$ (JCPDS no. 42-1450). The XRD pattern of CCS also consists of some other peaks at 27.7°, 32.2° and 46.2°, which are matched with the Cu$_{2-x}$S (JCPDS no. 00-002-1281). The introduction of Fe in the CCS structure shifts the diffraction peaks towards a slightly lower angle than that in pristine CCS. This suggests that Fe^{3+} ions have been assimilated into the octahedral Co^{3+} sites. A greater interplanar distance results from the slightly increased ionic radius of Fe^{3+}, leading to a shift in the XRD peak to a lower 2θ value, in accordance with the Bragg's law.

Rietveld refinement of CuCo$_2$S$_4$ and Fe-doped CuCo$_2$S$_4$

The XRD patterns of CuCo$_2$S$_4$ and Fe-doped CuCo$_2$S$_4$ were analyzed by multiphase Rietveld refinements with the Fullprof program employing the pseudo-Voigt axial divergence asymmetry function. The cubic structure with the $Fd\bar{3}m$ space group is successfully refined from all peaks of CuCo$_2$S$_4$ and Fe-doped CuCo$_2$S$_4$. Less than 6% Cu$_2$S ($Fd\bar{3}m$) is quantified in CuCo$_2$S$_4$ and Fe-doped CuCo$_2$S$_4$, as shown in Fig. S1. Fe$_{0.01}$CCS doping results in 97% CuCo$_2$S$_4$ and 3% Cu$_2$S. The FeS phase ($P6_3/mmc$) is observed to segregate as the Fe doping increases, leading to a quantification of less than 5%. A slight decrease in the unit cell dimension is observed from CuCo$_2$S$_4$ (9.47 Å) to Fe$_{0.01}$CCS (9.46 Å) (Table S2). This decrease is attributed to the occupancy of Fe at the octahedral site. Further, the addition of Fe increases the phase segregation, which leads to the formation of FeS, resulting in less occupancy of Fe at the octahedral site of CuCo$_2$S$_4$. The Fe$_{0.01}$CCS and Fe$_{0.03}$CCS exhibit a negative shift in the 2θ value (a shift to lower 2θ values) for the (224), (044), and (117) planes. This suggests that Fe^{3+} ions have been assimilated into the octahedral Co^{3+} sites. A greater interplanar distance results from the slightly increased ionic radius of Fe^{3+}, leading to a shift in the XRD peak to a lower 2θ value, in accordance with the Bragg's law. With the exception of one plane (224), where there is no 2-theta shift in Fe$_{0.05}$CCS and a lower 2-theta shift in Fe$_{0.07}$CCS, whereas all other planes shift to higher 2-theta in both samples (Table S3 in SI).

The intensity of the (111) plane is given as 16.63 in the standard JCPDS 042-1450 and decreases to 16.24 in the pure CuCo$_2$S$_4$, according to the intensity value of 100 for the (113) plane. The percentage change in relative intensity is displayed in Table S4, where a decrease in intensity is indicated by a negative sign and an increase in intensity relative to the standard JCPDS is indicated by a positive sign. An increase in peak intensity is shown by the (135) and (117) planes of pure CuCo$_2$S$_4$ and Fe$_{0.03}$CCS, the (117) plane of Fe$_{0.01}$CCS, the (111) and (117) planes of Fe$_{0.05}$CCS, and the (111), (044), (135), and (117) planes of Fe$_{0.07}$CCS. The increased intensity suggests that doped Fe^{3+} may exist in the interstitial voids. The peaks that show a decrease in intensity can be attributed to the inclusion of Fe^{3+} at the octahedral site of Co^{3+}, as a slightly weaker scattering effect is produced by Fe^{3+} than by Co^{3+}. The decrease in peak intensity may also be caused by the sulphur point defects. The surrounding metal cations (Co^{3+} and Cu^{2+}) capture the

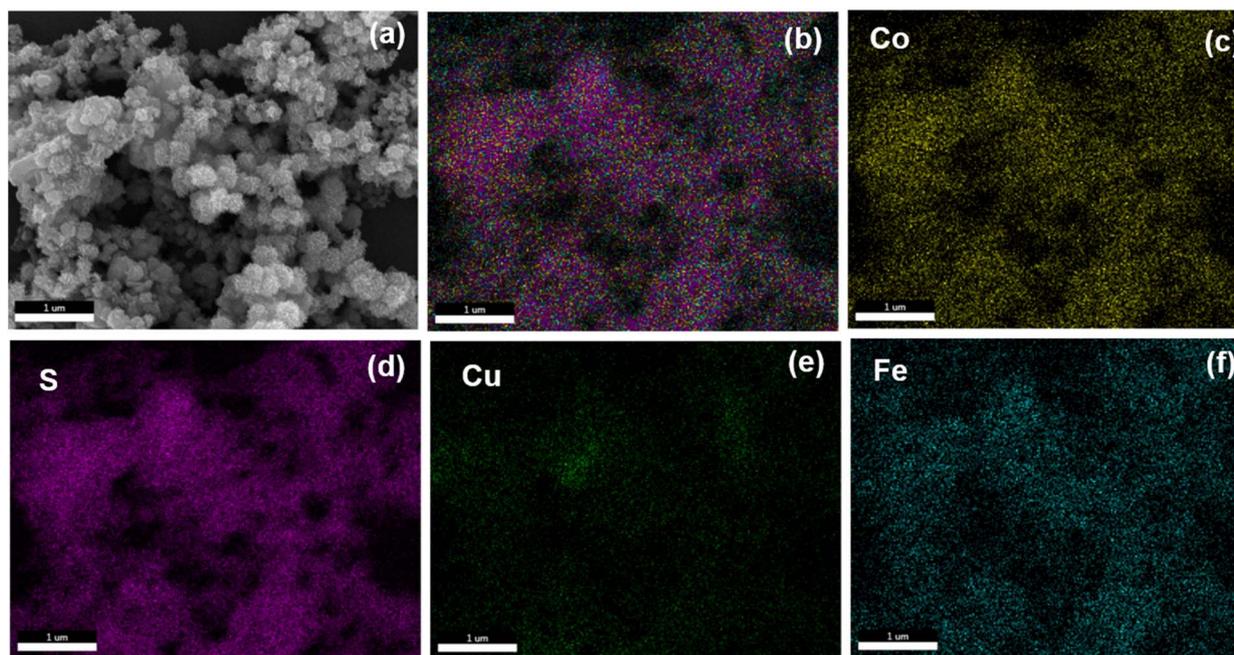This journal is © The Royal Society of Chemistry 2026

J. Mater. Chem. A, 2026, 14, 2218–2234 | 2221

Fig. 3 FESEM image at 1 μm of (a) $Fe_{0.03}CCS$. (b) SEM EDS mappings of $Fe_{0.03}CuCo_2S_4$, (c) Co, (d) S, (e) Cu and (f) Fe.

trapped electrons from the sulphur vacancies, reducing Co^{3+} to Co^{2+} and Cu^{2+} to Cu^+. This reduction causes an increase in the d-spacing due to the larger ionic radii of Co^{2+} and Cu^+ compared with those of Co^{3+} and Cu^{2+}, respectively, and results in negative 2θ shifts in XRD.

The chemical nature of the samples was further investigated using Raman spectroscopy. Fig. 2(c) shows the Raman spectrum of undoped $CuCo_2S_4$, and the peaks observed at 463.7, 503.9 and 601.6 cm^{-1} correspond to the E_g, A_{1g} and F_{2g} modes of the Co–S bond, respectively,[25] while the peak observed at 670.5 cm^{-1} corresponds to the F_{2g} mode of the S–S bond.[29] The addition of Fe in the pristine CCS structure results in a red shift (toward lower wavenumbers) for all peaks, implying the lattice distortion in the crystal structure.[30] The red shift increases with an increase in the Fe content. More lattice distortion is introduced in the crystal structure with Fe insertion, confirming the XRD results.

The morphology of the synthesized catalyst was studied by field-emission scanning electron microscopy (FESEM). The FESEM images of pure CCS show a nanosheet-type morphology (Fig. S2). These nanosheets are not interconnected to each other, and some nanosheets are flat on the substrate. The Fe doping of the pristine structure has no effect on the morphology (Fig. 3(a) and S2). The morphology after Fe addition remains the same. Fig. 3(b) shows the EDS mapping of $Fe_{0.03}CCS$, which demonstrates the homogeneous distribution of the elements Co, Cu, S and Fe.

Furthermore, transmission electron microscopy was employed to study the detailed interior structure of the catalyst. Fig. 4(a) presents the bright-field TEM image of $Fe_{0.03}CCS$ at a 200 nm magnification, which displays its 2D nanosheet morphology. In HRTEM analysis, we found that the flat surfaces

are predominantly exposed to the (111) plane. In some cases, the perpendicular surfaces are exposed to the (311) and (004) planes (Fig. 4(b)). Fig. 4(c) shows the selected area electron diffraction (SAED) with the ring pattern, indicating the polycrystalline nature of the catalyst. The SAED pattern contains the diffractions from the (111), (022), (113), (004), (115), and (044) planes of CCS, which is consistent with the XRD result. Further, Fig. 4(d) presents the HRTEM image of CCS, showing a perpendicular sheet with a reflection from the (004) plane.

The XPS survey spectrum shows the signals of Cu, Co, S, N and C for CCS, while for Fe-doped samples, the signal corresponding to Fe is also present without any additional peaks, demonstrating the purity of the synthesized catalyst (Fig. 5(a) and (b)). The deconvolution of the Co 2p spectra displays two doublets corresponding to Co $2p_{3/2}$ and Co $2p_{1/2}$. The deconvoluted spectra show the peaks at 778.64 eV and 793.7 eV, which are the characteristic peaks of Co^{3+}, while the peaks at 780.5 and 796.1 eV correspond to Co^{2+} (Fig. 5(c)). Two satellite peaks are also present in the deconvoluted data, corresponding to Co $2p_{3/2}$ and Co $2p_{1/2}$. Upon Fe doping, the XPS spectra of the doped samples show almost negligible change in the Co 2p spectra (Fig. S3(a)). Similarly, the Cu 2p spectra are deconvoluted into two doublets due to spin–orbit coupling. The peaks at 932.3 and 952.1 eV are attributed to Cu^{1+}, while the peaks at 934.2 and 955.5 are attributed to Cu^{2+} (Fig. 5(d)). The addition of Fe in the CCS structure shows no change in the XPS spectra (Fig. S3(b)). The S 2p peaks are deconvoluted into a satellite peak (168.7 eV) and three peaks. The peaks at 161.6 and 162.7 eV are ascribed to S $2p_{3/2}$ and S $2p_{1/2}$, respectively. The peak at 164.1 eV suggests the presence of the sulfur–metal (S–M) bond (Fig. 5(e)). The deconvoluted Fe spectra show two spin–orbit doublets corresponding to $2p_{3/2}$ and $2p_{1/2}$. The peaks at 710.7 and 732.8 eV
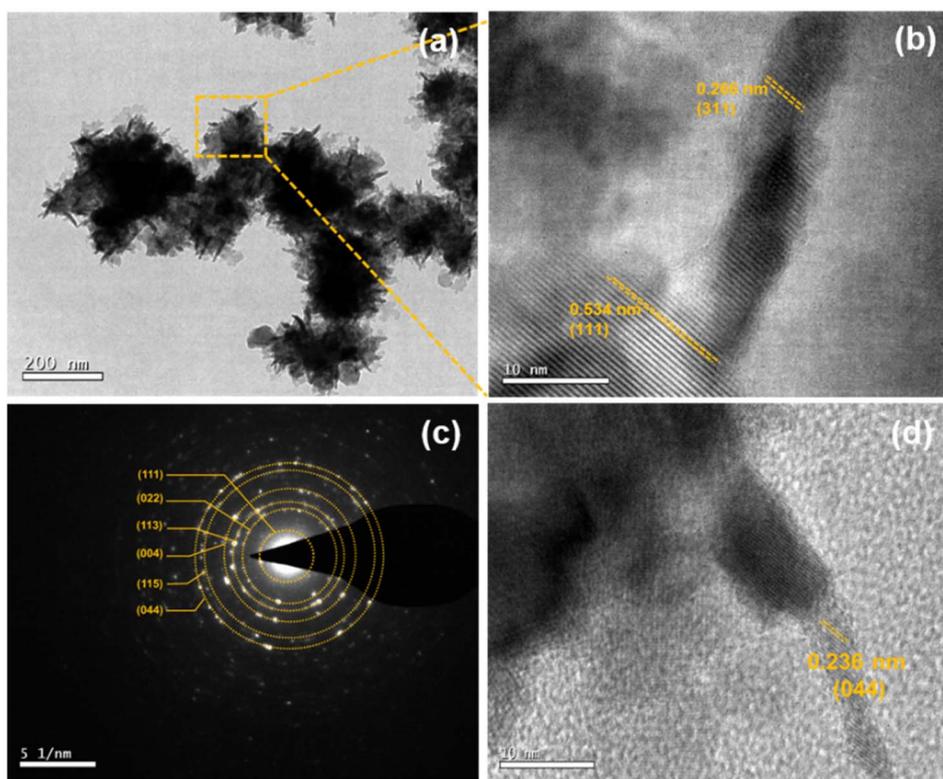
2222 | J. Mater. Chem. A, 2026, 14, 2218–2234

This journal is © The Royal Society of Chemistry 2026

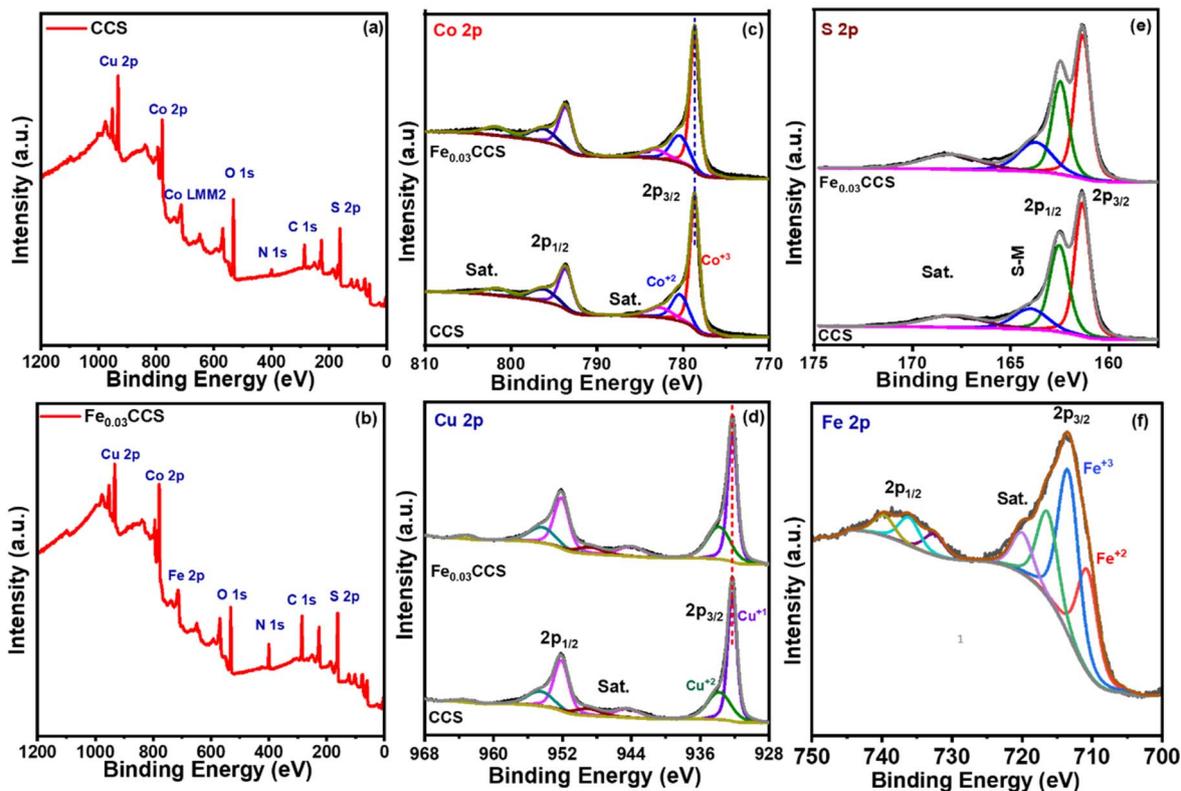Fig. 4 (a) Low-magnification TEM image of $Fe_{0.03}CCS$. (b) HRTEM image of $Fe_{0.03}CCS$. (c) SAED pattern of $Fe_{0.03}CCS$. (d) HRTEM image of CCS.

Fig. 5 XPS survey spectrum of (a) CCS and (b) $Fe_{0.03}CCS$. Deconvoluted XPS spectra of CCS and $Fe_{0.03}CCS$: (c) Co 2p, (d) Cu 2p and (e) S 2p. (f) Deconvoluted XPS spectra of Fe 2p for the $Fe_{0.03}CCS$ catalyst.

This journal is © The Royal Society of Chemistry 2026

J. Mater. Chem. A, 2026, 14, 2218–2234 | 2223

correspond to Fe^{2+}, while the peaks at 713.4 and 736.1 eV represent Fe^{3+} (Fig. 5(f) and S3(d)). XPS depth profiling was also performed to investigate the elemental distribution from the surface to the bulk phase for Co 2p, Cu 2p, Fe 2p and S 2p by sequential etching for 60 s and 120 s, as shown in Fig. S4–S7. After etching, the S 2p peak exhibits a slight shift toward higher binding energies, accompanied by the diminution of the satellite peak. This behavior suggests the removal of surface-adsorbed or reduced sulfur species and the exposure of more stoichiometric lattice sulfur. Meanwhile, the Fe 2p, Co 2p, and Cu 2p spectra show no significant change in binding energy, but their intensities increase after etching, indicating that the oxidation states of the metal cations remain stable and that Fe is homogeneously distributed throughout the structure without surface segregation.

The electrochemical ORR activity of all samples was first examined by CV in N_2 and then in an O_2-saturated 0.1 M KOH electrolyte over a wide potential range from 0.16 to 1.16 V vs. RHE at a scan rate of 20 mV s^{-1}. As shown in Fig. S8(a), a featureless CV is observed in an N_2 environment; however, subsequent studies in O_2-saturated 0.1 M KOH demonstrate a steep increase in the reductive current density, ascribed to ORR activity. Further, to gain insights into the ORR mechanism and kinetics, detailed experiments were performed under hydrodynamic conditions, viz., RDE and RRDE measurements.

The RDE linear polarisation curves of various catalysts at a rotation rate of 1600 rpm at 5 mV s^{-1}, as shown in Fig. 6(a), demonstrate a good onset potential and a high diffusion-limited current density for all the catalysts. Remarkably, the optimized $Fe_{0.03}CCS$ shows comparable onset (0.89 V) and half-wave potentials (0.80 V), respectively, and a higher diffusion-limited current density (Fig. 6(a)). Fig. 6(b) presents the bar graph comparison of the onset and half-wave potentials of all the catalysts. The $Fe_{0.03}CCS$ catalyst performs better than other catalysts but still poorer than the commercial Pt/C. To gain a deeper insight into the ORR, the RRDE measurements were conducted at different rotation rates from 225 to 1600 rpm at a 5 mV s^{-1} scan rate (Fig. 6(c) and S8(c–l)). With an increase in the rotation rate, the reduction current density increases, which indicates the faster diffusion of oxygen on the surface of the catalyst with an increase in the mass transport current. To determine the mechanistic pathway for the ORR, Koutecky–Levich (K–L) plots, derived from the RDE measurements at different potentials (Fig. 6(c) and S8), were plotted, which show good linearity between the reverse square root of rotation and reverse current density, confirming the first-order kinetics for ORR process. Fig. 6(d) shows the ORR durability test. The ORR durability tests were performed by running the CV in the potential range from 1.01 to 0.61 V vs. RHE at a 100 mV s^{-1} scan rate for 1000 cycles, followed by LSV at 5 mV s^{-1}. The LSV curves before and after the durability test show only a 17 mV shift in the half-wave potential with a slight decrease in the current density.

Moreover, the $Fe_{0.03}CCS$ shows excellent methanol tolerance and exhibits greater stability (Fig. 6(e)). Fig. 6(f) shows the number of electrons transferred and H_2O_2 production yield for CCS and $Fe_{0.03}CCS$ calculated at different potentials from 0.3 V to 0.7 V vs. RHE from the LSV curves of the RRDE. The number of electrons transferred for the ORR process is close to 4, while

the H_2O_2 production yield is less than 5%. The number of electrons transferred was calculated from the RRDE plot and is found to be ca. 3.98 for $Fe_{0.03}CCS$, with an average H_2O_2 production of 0.5–10%.

To probe the bifunctional activity, the OER activity of all the catalysts was evaluated by performing LSV at 5 mV s^{-1} in the potential range from 1.20 V to 1.82 V vs. RHE. The OER activity was studied in a 1 M KOH solution in a N_2-saturated environment; all the catalysts were examined by cyclic voltammetry in a wide potential range from 0.02 V to 1.62 V at a scan rate of 50 mV s^{-1} (Fig. S9(a)). Fig. 6(g) shows the OER polarization curve of all the catalysts at a scan rate of 5 mV s^{-1}. The $Fe_{0.03}CCS$ has a better onset potential than CCS and other Fe-doped catalysts for the OER. Fig. 6(h) shows the bar graph comparison for the OER at different current densities for all the synthesized catalysts and RuO_2. The $Fe_{0.03}CCS$ catalyst has the lowest overpotential (330 mV) at a 10 mA cm^{-2} current density.

Moreover, the current density of $Fe_{0.03}CCS$ is far greater than that of CCS. The $Fe_{0.03}CCS$ has a lower overpotential at 10 mA cm^{-2} than other synthesized catalysts. The Tafel plot was also determined from the corresponding polarization curves (Fig. 6(i)). The $Fe_{0.03}CCS$ has a lower Tafel slope (69.9 mV dec^{-1}) and faster kinetics for the OER compared to CCS (79.8 mV dec^{-1}). Fig. 6(j) shows the Nyquist plot for the prepared catalysts. All the catalysts have a similar solution resistance (R_s), as electrochemical studies were performed at the same electrolyte concentration. The $Fe_{0.03}CCS$ shows a lower value of charge transfer resistance than the pristine CCS catalyst. The acceleration durability test (ADT) was also conducted to study the long-term durability of the $Fe_{0.03}CCS$ catalyst. The ADT was performed from 1.04 V to 1.62 V vs. RHE at 100 mV s^{-1} (Fig. 6(k) and S9(b)). Initial cycles show quite good stability with an increase in the oxidation state, and even after 500 cycles, the OER performance shows greater stability (Fig. 6(l)).

The electrochemical double-layer capacitance (C_{dl}) was estimated by cyclic voltammetry in the potential window from 1.12 V to 1.22 V vs. RHE at different scan rates from 10 to 100 mV s^{-1} (Fig. S9(c–l)). Double-layer capacitance was determined from the slope of the current density vs. scan rate plot. Fig. 7(a) shows the C_{dl} values of all the prepared catalysts, with $Fe_{0.03}CCS$ having the highest value of C_{dl} at 28.84 mF compared with the pristine CCS (6.02 mF). The long-term stability was studied via chronoamperometry at a 10 mA cm^{-2} current density on the carbon paper (Fig. 7(b)). Fig. 7(b) shows the chronoamperometry study's results at 10 mA cm^{-2} for 24 h, which exhibits the stable nature of the catalyst with a minimal reduction in the current density. The post catalysis analysis was also performed before and after the chronoamperometry study. The XRD and Raman spectra show no change in the peaks before and after the chronoamperometric test, indicating the good recyclability of the catalyst (Fig. 7(d) and (e)). The excellent oxygen electrocatalytic activity of the $Fe_{0.03}CCS$ catalyst makes it a potential candidate as an air electrode for metal–air batteries. The difference in the potential (ΔE) (where $\Delta E = E_{j=10 \text{ mA cm}^{-2}(\text{OER})} - E_{1/2(\text{ORR})}$, where $E_{j=10}$ is the potential required to produce a 10 mA cm^{-2} current density during the OER and $E_{1/2}$ is the half-wave potential for the ORR) is the measure of the

2224 | J. Mater. Chem. A, 2026, **14**, 2218–2234

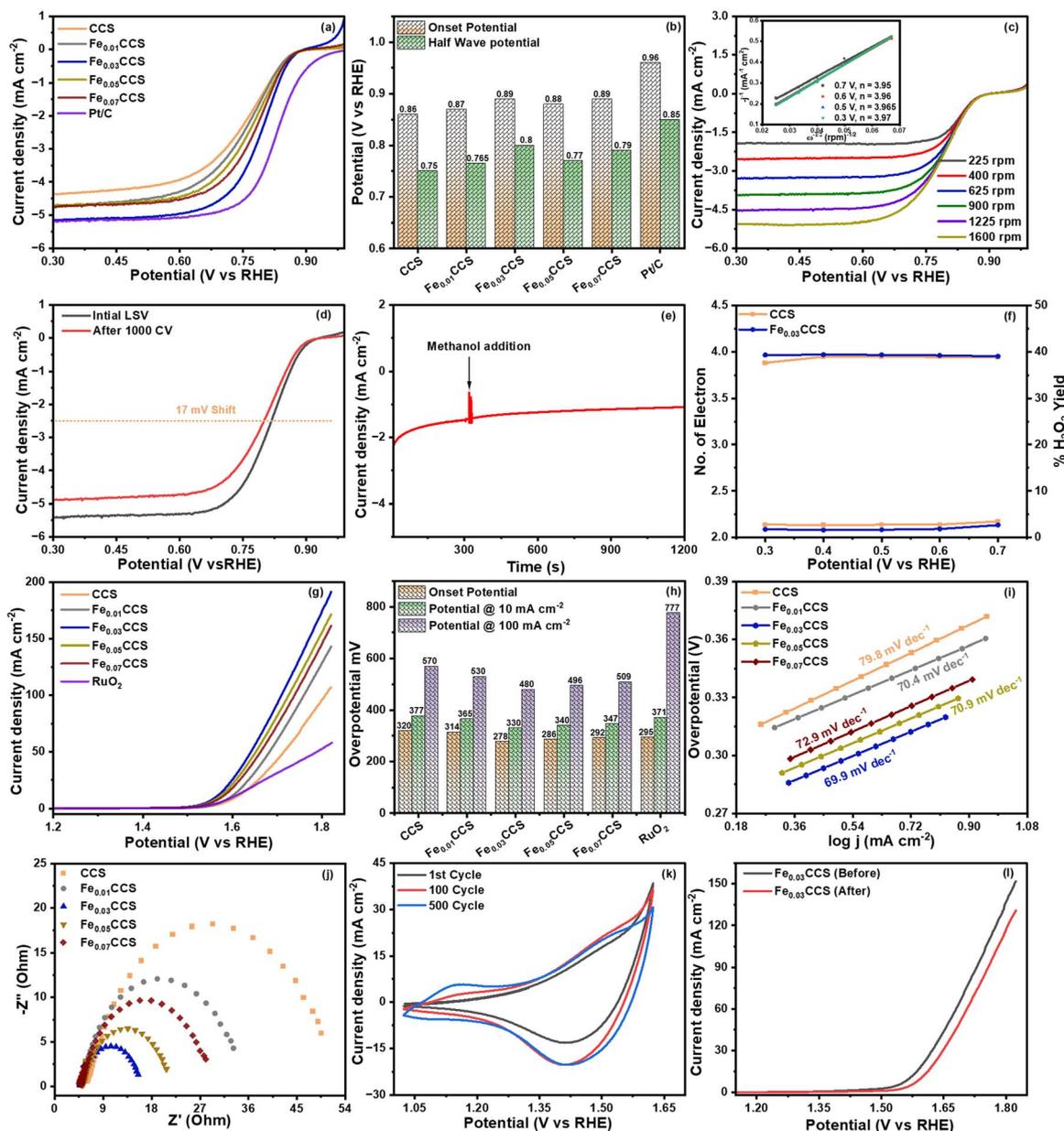This journal is © The Royal Society of Chemistry 2026

Fig. 6 (a) ORR comparison plots of all the synthesized catalysts and 20% Pt/C in oxygen-saturated 0.1 M KOH at 1600 rpm in the potential window from 0.3 to 1 V vs. RHE at a scan rate of 5 mV s^{-1}. (b) Bar graph comparison of all the synthesized catalysts and 20% Pt/C. (c) LSV plot of Fe$_{0.03}$CCS at different rotation rates from 225 to 1600 rpm at a 5 mV s^{-1} scan rate, with the inset showing the Koutecky–Levich plot for the Fe$_{0.03}$CCS catalyst at various potentials and the number of electrons transferred. (d) ORR polarization comparison of Fe$_{0.03}$CCS after cycling in oxygen-saturated 0.1 M KOH for 1000 cycles. (e) Methanol tolerance test of the Fe$_{0.03}$CCS catalyst. (f) Number of electrons transferred and H$_2$O$_2$ percentage yield of CCS and Fe$_{0.03}$CCS at different potentials based on the RRDE data. (g) OER comparison plot of all the synthesized catalysts and RuO$_2$ in 1 M KOH at 1600 rpm in the potential window from 1.2 to 1.82 V vs. RHE. (h) Bar graph comparison of all the synthesized catalysts for the OER at different current densities. (i) Tafel plot with the corresponding Tafel slope values for all the synthesized catalysts. (j) Nyquist plot. (k) Acceleration durability test showing 1st, 100th and 500th cycles. (l) LSV polarization comparison of Fe$_{0.03}$CCS after cycling in nitrogen-saturated 1 M KOH for 500 cycles.

bifunctional activity of the oxygen electrocatalyst. The smaller value of ΔE indicates the improved bifunctionality of the Fe-doped spinel. Fig. 7(f) shows the bifunctional activity bar graph for all the catalysts, and the Fe$_{0.03}$CCS catalyst shows the lowest ΔE value of 0.76 V, indicating its superiority over the other catalysts. Table S5 presents the $E_{1/2(\text{ORR})}$, $E_{j=10 \text{ mA cm}^{-2}(\text{OER})}$ and ΔE values of various catalysts reported, showing that our

catalyst exhibits greater performance compared to other catalysts.

All state Zn–air battery testing

In order to assess Fe$_{0.03}$CCS's possible use in storage devices, we built a standard Zn–air battery and measured its battery performance in an alkaline medium. The aqueous battery was
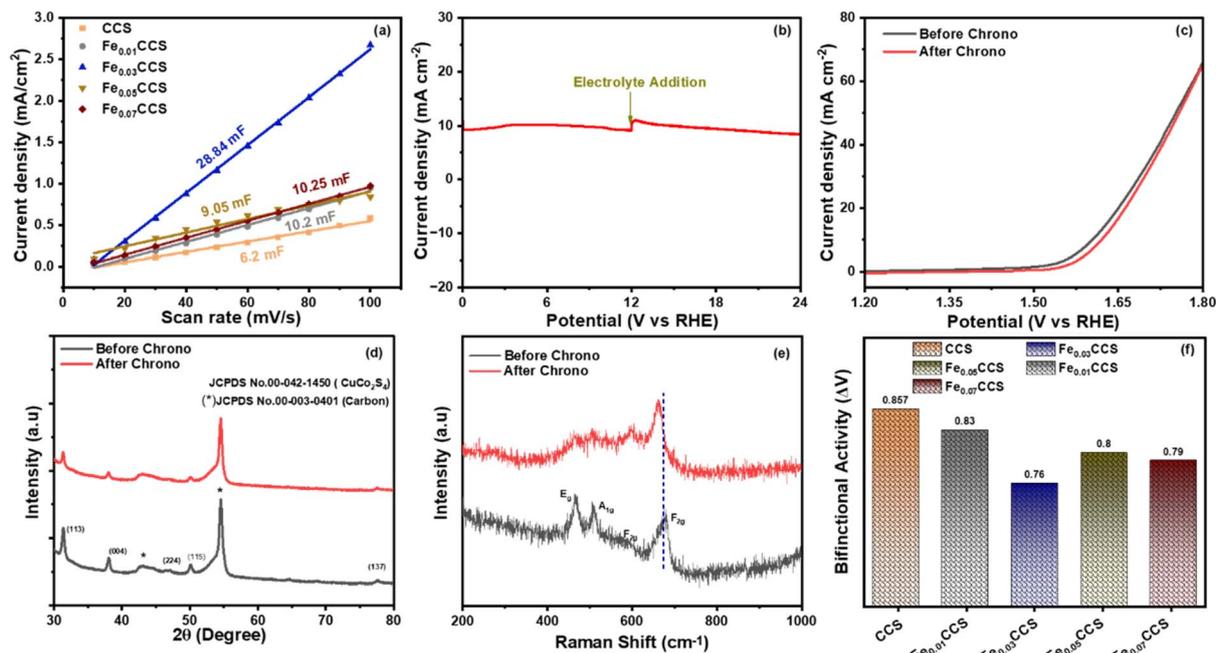
This journal is © The Royal Society of Chemistry 2026

J. Mater. Chem. A, 2026, **14**, 2218–2234 | **2225**

Fig. 7 (a) Electrochemically active surface area (ECSA) of all the synthesized catalysts in the EDLC region. (b) Chronoamperometric response of $Fe_{0.03}CCS$ in nitrogen-saturated 1 M KOH. (c) LSV polarization comparison of $Fe_{0.03}CCS$ before and after the chronoamperometry study. (d) XRD patterns before and after the 24 h chronoamperometry study. (e) Raman spectra before and after the 24 h chronoamperometry study. (f) Bifunctional activity bar graph of all the synthesized catalysts.

assembled using a $Fe_{0.03}CCS$ air cathode and a Zn foil anode in a 6 M KOH + 0.2 M zinc acetate electrolyte. For comparison, a pristine CCS catalyst-based zinc–air battery was also made. The open-circuit potential of the $Fe_{0.03}CCS$-based battery is approximately 1.43 V, as shown in Fig. 8(a), and it stays constant even after 24 hours, while the pristine CCS battery shows an OCP value of 1.35 V. The battery's energy storage capacity, measured at 5 mA cm^{-2}, shows a voltage platform at 1.20 V, resulting in a specific capacity of 803.4 mA h g^{-1}, normalized with the mass of lost zinc, and the CCS-based battery has a value of 748.8 mA h g^{-1} (Fig. 8(b)). Fig. 8(b) inset shows the bar graph of the discharge test of the $Fe_{0.03}CCS$ aqueous zinc–air battery at different current densities ranging from 2 to 20 mA cm^{-2}. The specific capacity of the aqueous zinc–air battery was calculated by discharging at a specific current density and regularized using the weight of zinc consumed in the process. The specific capacities at 2 mA cm^{-2}, 5 mA cm^{-2}, 10 mA cm^{-2} and 20 mA cm^{-2} are 804.1 mA h g^{-1}, 801.9 mA h g^{-1}, 799.8 mA h g^{-1} and 793.6 mA h g^{-1}, respectively (Fig. S10(a)). Fig. 8(c) shows the step discharge for both the catalysts, CCS and $Fe_{0.03}CCS$, at various current densities ranging from 1 to 20 mA cm^{-2}. The discharge potential of CCS decreases more than that of $Fe_{0.03}CCS$ when the current density reaches 20 mA cm^{-2}. The peak power density of the $Fe_{0.03}CCS$ catalyst is 82 mW cm^{-2}, and the peak power density of CCS is only 52 mW cm^{-2}, as illustrated in Fig. 8(d). Furthermore, the efficiency and long-term durability were investigated by galvanostatic charge–discharge at a constant current density of 5 mA cm^{-2} for 10 minutes for charging and −5 mA cm^{-2} for 10 minutes for discharging (Fig. 9(a)).

More importantly, a negligible fading in the performance is observed even after 75 h and 210 cycles. During the initial period of battery operation, the voltage gap is low, with a high round-trip efficiency of 61.7% (Fig. 9(b)). After 100 cycles of GCD, the voltage gap increases to 0.88 V with a round-trip efficiency of 56.65% (Fig. 9(c)). For comparison, the galvanostatic charge–discharge performance of CCS was also studied under similar conditions. In contrast, in the CCS-based battery, the voltage gap increases drastically after 60 hours, showing poor oxygen bifunctional activity.

Most of the research articles reported on zinc–air batteries have only evaluated the galvanostatic charge–discharge for 20 minutes per cycle. To evaluate the performance for practical applications, it is necessary to conduct longer charge–discharge tests as during longer discharge times, the zincate ion gets saturated and forms the insoluble zinc oxide in the electrolyte, which restricts the performance of the zinc–air battery. However, during longer charging times, dendritic growth increases, which increases the voltage during charging.

To study the effect of longer charge–discharge times, we conducted galvanostatic charge–discharge at 4 h per cycle and 6 h per cycle. During the 4 h per cycle test, the battery can easily run for 54 hours, with a small increase in the voltage gap, a lesser amount of zinc oxide formation and a lower increase in polarization (Fig. 9(d)). By contrast, during the 6 h per cycle test, the initial 8 cycles show a smaller voltage gap and the battery runs for 50 hours (Fig. 9(e)). After this, both the charging and discharging voltages start increasing, showing the effects of dendritic growth and the formation of zinc oxide in the electrolyte, respectively. The discharging voltage increases more
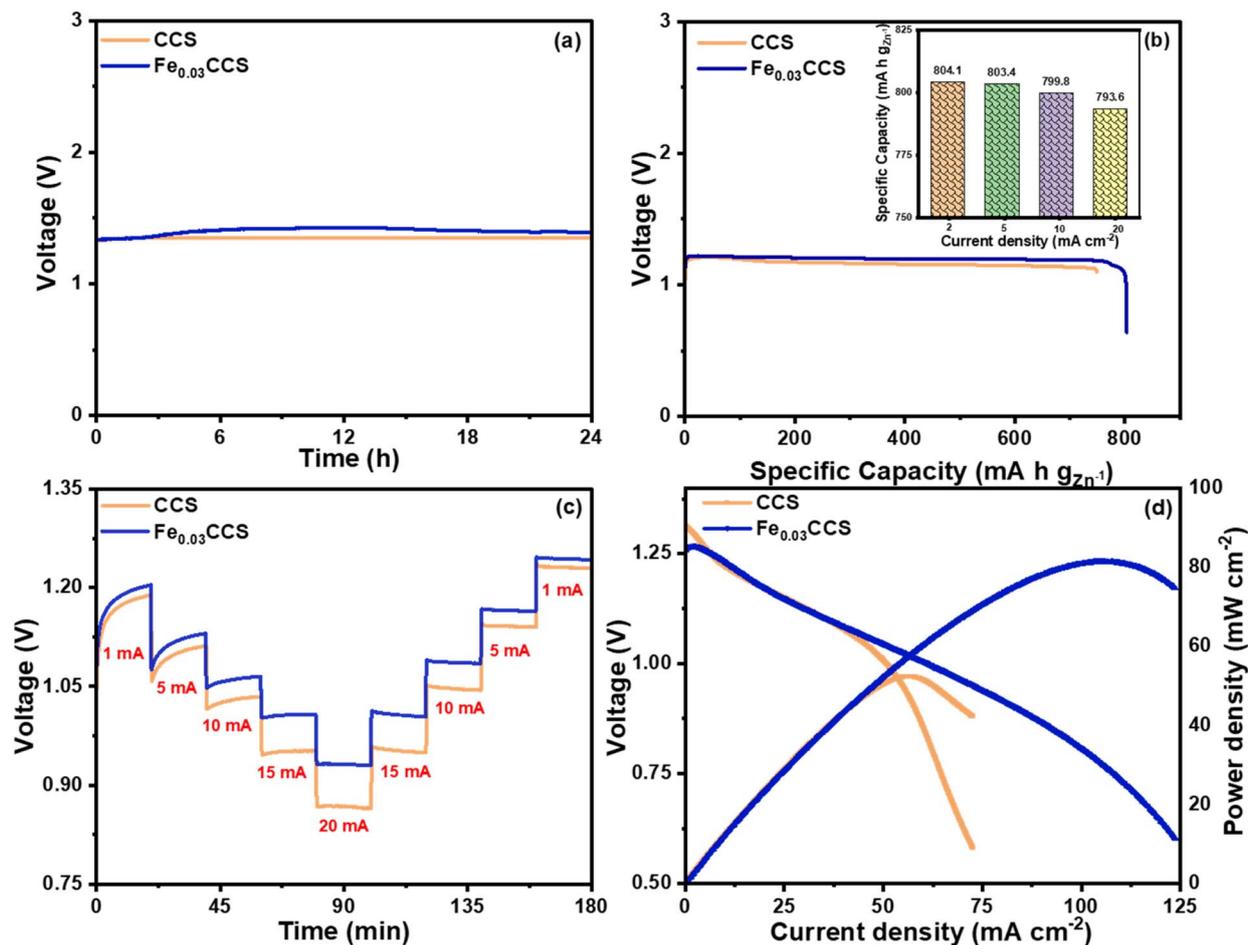
2226 | J. Mater. Chem. A, 2026, **14**, 2218–2234

This journal is © The Royal Society of Chemistry 2026

Fig. 8 Aqueous Zn–air battery performance using CCS and $Fe_{0.03}CCS$ as air cathodes: (a) open-circuit potential and (b) specific capacity at a 5 mA cm^{-2} current density (inset shows a bar graph of the aqueous zinc–air battery at different current densities ranging from 2 to 20 mA cm^{-2}). (c) Step discharge at various current densities ranging from 1 to 20 mA cm^{-2}. (d) Discharge polarisation curves and the corresponding power densities.

than the charging voltage, which indicates the effect of the increased passivation of zinc oxide.

Furthermore, a solid-state zinc–air battery composed of the $Fe_{0.03}CCS$ catalyst was assembled using a solid-state polymer as an electrolyte. Fig. 10 shows the digital photographs of the foldable ZABs at different bending angles used to light an LED lamp. Discharge–charge curves of $Fe_{0.03}CCS$ in foldable ZABs at various bending angles show that the battery is efficient at all bending angles.

The assembled solid-state zinc–air battery shows an OCP value of 1.37 V, which is slightly less than that of the aqueous battery due to the internal resistance of the solid-state electrolyte (Fig. 11(a)). When the two solid-state batteries are connected in series, the OCP value almost doubles to 2.706 V (Fig. 11(b)). Using two solid-state batteries, we can light an LED, providing a real-life demonstration of our catalyst (Fig. 11(c)). Fig. 11(d) shows the galvanostatic charge–discharge plot of the $Fe_{0.03}CCS$ catalyst at 2 mA cm^{-2} with a 5 min charge and 5 min discharge cycle. The GCD shows stability for 25 h with a small change in the voltage gap, showing the good durability of our catalyst under the solid-state condition.

Additionally, Fig. 11(e) shows the specific capacity of the $Fe_{0.03}CCS$ catalyst at 5 mA cm^{-2}. The zinc foil was mechanically scratched, and the amount lost was used to calculate the specific capacity of the solid-state battery. Additionally, we performed the discharge testing of the $Fe_{0.03}CCS$ solid-state zinc–air battery at various current densities from 1 to 10 mA cm^{-2} (Fig. S10(b)). Fig. 11(f) shows the step discharge of the solid-state battery at different current densities ranging from 0.5 mA to 5 mA cm^{-2}. The step discharge of the $Fe_{0.03}CCS$ catalyst shows its good stability at all current densities and better reversibility. The $Fe_{0.03}CCS$ catalyst shows promising behavior for real-life zinc–air battery applications. These results illustrate that $Fe_{0.03}CCS$ is a promising alternative to noble metal-based catalysts and can be successfully used as an air cathode for Zn–air batteries.

Theoretical analysis

In order to have a deeper understanding of the underlying mechanism of the electrocatalytic OER-ORR performance on the $CuCo_2S_4$ (113) surface, we performed first-principles

This journal is © The Royal Society of Chemistry 2026

J. Mater. Chem. A, 2026, **14**, 2218–2234 | **2227**

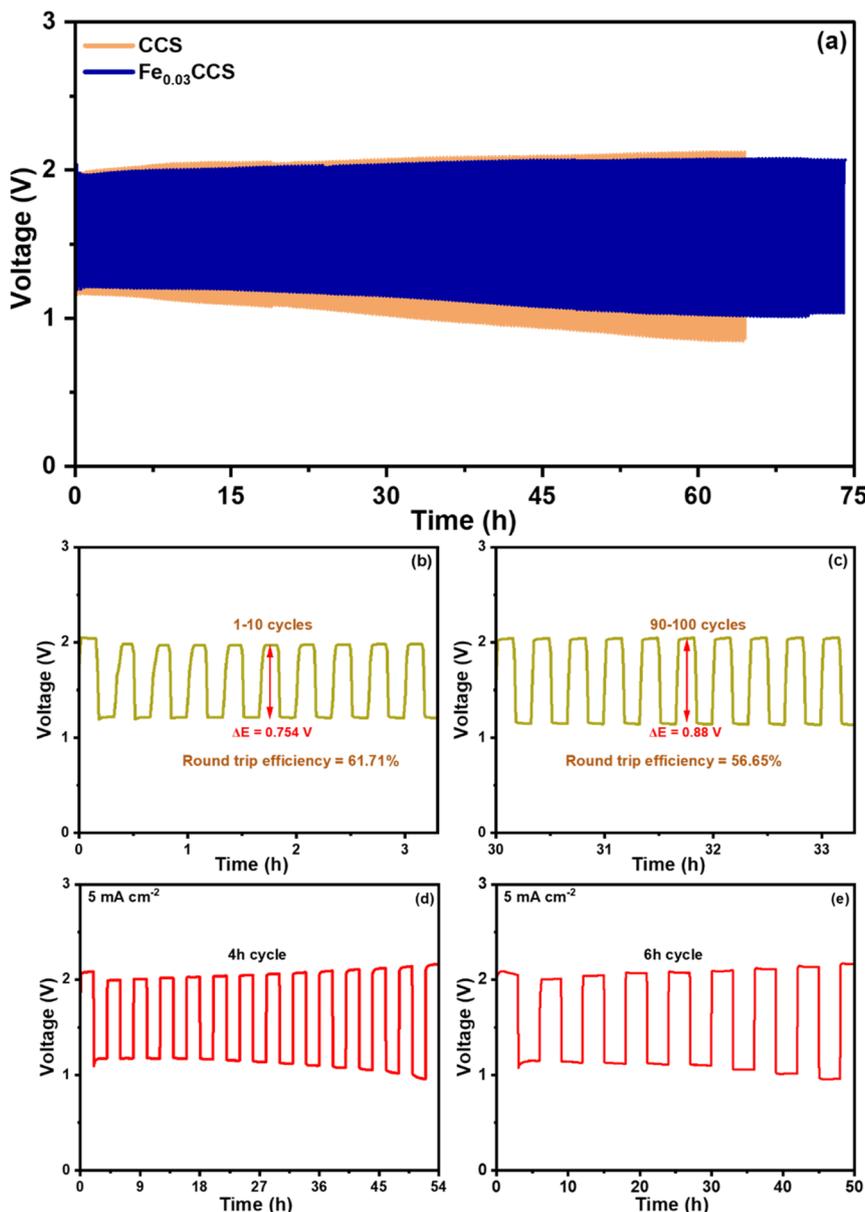**Fig. 9** (a) Galvanostatic charge–discharge curve at 5 mA cm^{-2} in a 10 minutes charge–discharge cycle. (b) and (c) Corresponding round-trip efficiency calculation during 1–10 cycles and 90–100 cycles, respectively. Galvanostatic charge–discharge plot of the Fe$_{0.03}$CCS zinc–air battery at a current density of 5 mA cm^{-2} with (d) 4 h per cycle and (e) 6 h per cycle tests.

calculations under the framework of the density functional theory (DFT). To model the experimentally synthesized structure, we cleaved the (113) plane of both pristine CuCo$_2$S$_4$ (CCS) and Fe-doped CuCo$_2$S$_4$ [Fe$_x$CuCo$_2$S$_4$] surfaces from the bulk.

Our theoretical investigation of the OER-ORR activity was mainly based on Nørskov's approach[31] of reaction coordinate mapping. According to this approach, for a good OER-ORR catalyst, all the reaction steps involved in the process should have a free energy change (ΔG) close to 1.23 eV, as the redox potential for water splitting is 1.23 V. This ensures that the catalyst will bind with reaction intermediates (O*, OH*, and OOH*) neither too strongly nor too weakly for the reaction to occur without applying a significant amount of external bias.

The free energy of the adsorbed intermediates on the catalyst surface can be determined using the following equation:

$$\Delta G_X^* = E_{ads}^X + \Delta ZPE - T\Delta S,$$

where X are the intermediates O*, OH* and OOH*, E_{ads}^X gives the adsorption energy of the intermediates, and ($\Delta ZPE - T\Delta S$) is the correction due to zero-point energy and entropic contribution between the adsorbed state and the free state of each intermediate.

The oxygen evolution reaction (OER) in aqueous solutions proceeds *via* the direct four-electron oxidation of water (H$_2$O) to oxygen (O$_2$), which leads to oxygen evolution.

2228 | *J. Mater. Chem. A*, 2026, **14**, 2218–2234
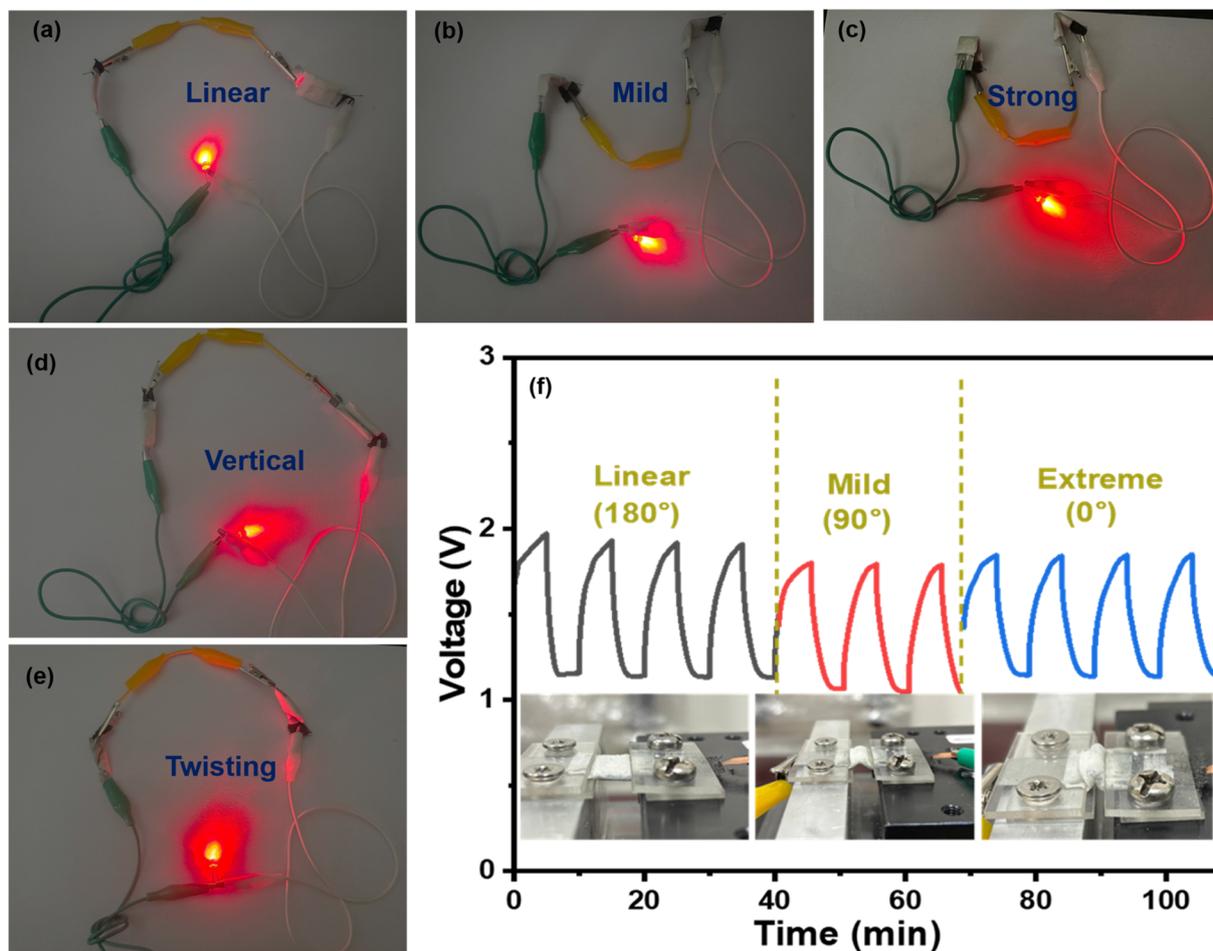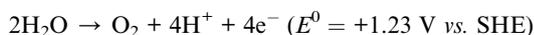
This journal is © The Royal Society of Chemistry 2026

Fig. 10 (a–e) Digital photographs of the foldable ZABs at different bending angles, lighting an LED lamp. (f) Discharge–charge curves of $Fe_{0.03}CCS$ in foldable ZABs at various bending angles.

$$2H_2O \rightarrow O_2 + 4H^+ + 4e^- \quad (E^0 = +1.23 \text{ V } vs. \text{ SHE})$$

The free energy change for the four elementary steps of OER can be obtained as follows: $\Delta G_1 = \Delta G_{OH^*} - \Delta G_{H_2O}$, $\Delta G_2 = \Delta G_{O^*} - \Delta G_{OH^*}$, $\Delta G_3 = \Delta G_{OOH^*} - \Delta G_{O^*}$, and $\Delta G_4 = \Delta G_{O_2} - \Delta G_{OOH^*}$. The maximum free energy change $\Delta G_{max} = \max [\Delta G_1, \Delta G_2, \Delta G_3, \Delta G_4]$ among these four steps defines the potential needed to make the OER thermodynamically favourable; *i.e.* all steps must be downhill. The extra potential is known as the overpotential, defined as the amount of extra potential (voltage) that must be applied beyond the thermodynamic equilibrium potential to drive the reaction. For the OER, the overpotential (η_{OER}) is given by the formula:

$$\eta_{OER} = \frac{\Delta G_{max}}{e} - 1.23$$

The free energy values on pristine and doped surfaces for the oxygen evolution reaction (OER) are summarized in Table 1.

From Table 1, it is observed that when we consider the pristine CCS surface, the Co site has a lower overpotential of 0.97 V compared to the 1.96 V on the top of Cu, which indicates

relatively poor OER performance on the Cu site. If Co acts as the active site, we need to apply at least 2.19 V bias to make all OER steps thermodynamically favourable, *i.e.* exothermic, which gives rise to an overpotential of 0.96 V. Fig. 12(a) and (b) show the corresponding free energy profiles for the OER on the pristine $CuCo_2S_4$ surface. From the table and the free energy profile, it can be inferred that the formation of OOH* is the potential-determining step with the largest positive ΔG_n value on both active sites.

By contrast, when we consider the doped surface, the overpotential values are found to decrease significantly on some of the active sites upon doping with Fe. For the doped surface also, the Co site turns out to be the best possible active site with the lowest overpotential among all considered active sites. Fig. 12(c) shows that the η_{OER} reduces from 0.96 V to 0.49 V on the top of Co, while a small change is observed in the case of Cu, which reduces from 1.96 V to 1.75 V (Fig. 11(d)). The Fe site performs better than Cu but poorer than Co, with an overpotential of 1.17 V (Fig. 11(e)). It is anticipated that the substitutional doping alters the local electronic structure, which has a direct impact on the electron transfer between the surface and adsorbate and hence facilitates the OER process. This result matches well with the experimental outcome, where the doped
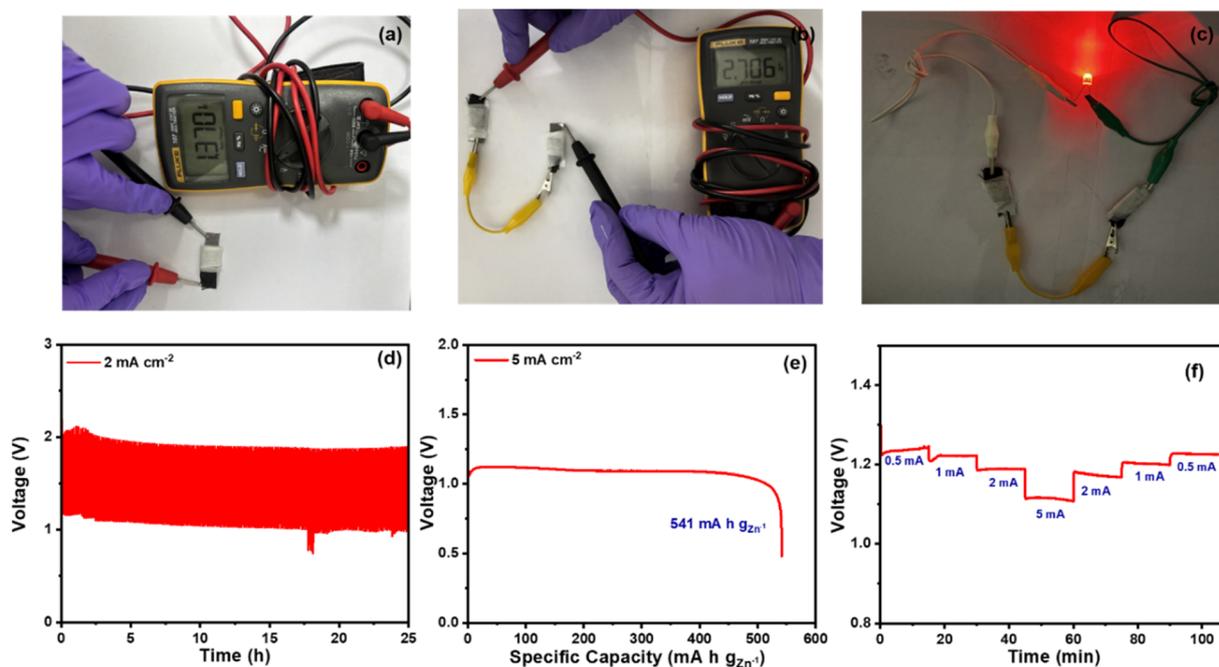
This journal is © The Royal Society of Chemistry 2026

J. Mater. Chem. A, 2026, **14**, 2218–2234 | **2229**

Fig. 11 (a) Assembly of the solid-state zinc–air battery composed of $Fe_{0.03}CCS$, with the OCP showing 1.37 V. (b) Two solid-state zinc–air batteries composed of $Fe_{0.03}CCS$ connected in series, with the OCP showing 2.706 V. (c) Image of the $Fe_{0.03}CCS$-based zinc–air battery-powered LED. (d) Galvanostatic charge–discharge curve of the solid-state zinc–air battery at a 2 mA cm^{-2} current density. (e) Plot showing the discharge capacity of the $Fe_{0.03}CCS$-based solid-state zinc–air battery at 5 mA cm^{-2}. (f) Step discharge of $Fe_{0.03}CCS$ at different discharge current densities.

surface is found to exhibit enhanced OER catalytic performance.

The oxygen reduction reaction (ORR), in which molecular oxygen (O_2) is reduced to water (H_2O), follows exactly the reverse steps of the OER while involving the same reaction intermediates, i.e. OH*, O* and OOH*.

$$O_2 + 4H^+ + 4e^- \rightarrow 2H_2O \ (E^0 = +1.23 \text{ V } vs. \text{ SHE})$$

Similar to the case of the OER, the free energy changes for the four elementary steps of the ORR can be obtained as follows: $\Delta G_1 = \Delta G_{OOH*} - \Delta G_{O_2}$, $\Delta G_2 = \Delta G_{O*} - \Delta G_{OOH*}$, $\Delta G_3 = \Delta G_{OH*} - \Delta G_{O*}$, and $\Delta G_4 = \Delta G_{H_2O} - \Delta G_{OH*}$. The theoretical overpotential for the ORR is calculated as follows:

$$\eta_{ORR} = \frac{\Delta G_{max}}{e} + 1.23V$$

The adsorption free energies for the ORR are summarized in Table 2.

Ideally, in the ORR, all the steps are exothermic at zero applied bias. When we studied the ORR mechanism on the pristine CCS surface, we observed that there exists no such adsorption site which can facilitate the process, with all four steps being exothermic at zero applied bias. It is evident from Table 2 that on Co and Cu active sites, ΔG_4 and ΔG_3 steps are uphill, respectively, indicating thermodynamically unfavourable ORR kinetics. Between Co and Cu, Co has the lower overpotential of 1.31 V.

By contrast, when we consider the ORR on the Co and Cu sites of the $Fe_xCuCo_2S_4$ surface, all four steps are found to have an exothermic nature at zero applied bias. Fig. 12(f) shows the free energy profile for the ORR on the Co active site of the doped $CuCo_2S_4$ surface. Cu, as an active site, has a slightly higher overpotential of 1.04 V than that of Co with an η_{ORR} value of ~0.81 V. By contrast, Fe shows poor catalytic performance for

Table 1 Gibbs free energy values for all the active sites on pristine and doped $CuCo_2S_4$ in the OER pathway

Surface(OER)	Active site*	ΔG_1 (eV)	ΔG_2 (eV)	ΔG_3 (eV)	ΔG_4 (eV)	η_{OER} (V)
$CuCo_2S_4$ (CCS)	Co	−0.08	0.95	2.19	1.84	0.96
	Cu	1.32	−0.51	3.19	0.93	1.96
$CuCoFeS_4$ ($Fe_xCuCo_2S_4$)	Co	0.42	1.42	1.72	1.36	0.49
	Cu	1.19	0.19	2.98	0.56	1.75
	Fe	−0.11	0.53	2.10	2.39	1.17

2230 | J. Mater. Chem. A, 2026, 14, 2218–2234
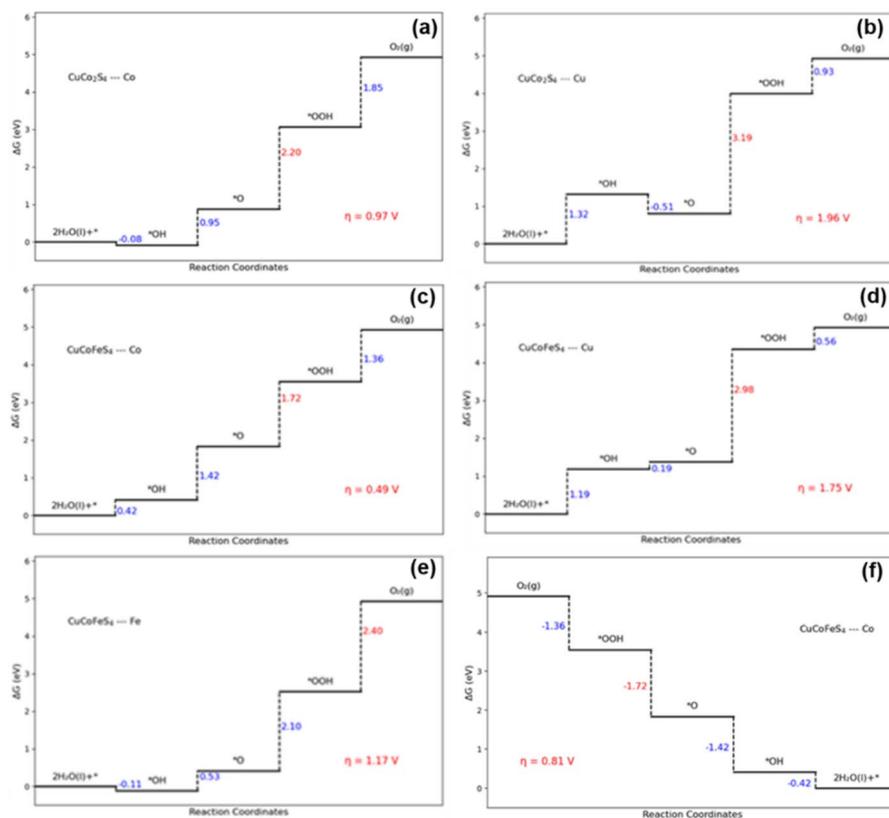
This journal is © The Royal Society of Chemistry 2026

Fig. 12 Free energy profile of (a) Co and (b) Cu active sites in $CuCo_2S_4$ for the OER mechanism. Free energy profile for $CuCoFeS_4$ for the OER mechanism on (c) Co, (d) Cu and (e) Fe active sites. (f) Free energy profile of the Co active site in $CuCoFeS_4$ for the ORR mechanism.

the ORR due to positive ΔG_4, which leads to a high overpotential of 1.34 V. This result suggests that Fe doping reduces the ORR overpotential on the Co site from 1.31 V on the pristine surface to 0.81 V on the doped surface by making the ΔG_4 step downhill. A similar observation is made for the Cu site, with the overpotential reducing from 1.74 V to 1.04 V, but by making ΔG_3 downhill. We calculated both the adsorption energy and free energy changes for the three reaction intermediates, namely, OH*, O*, and OOH* (where * represents the intermediate adsorbed on the catalyst surface), but in the table provided in the manuscript, only the free energy changes required to map the free energy profile diagram are given. We have also clearly mentioned both the adsorption energy and free energy changes for intermediate adsorption on both pristine and doped catalyst surfaces in Tables S6 and S7. The adsorption energy was calculated for the adsorption of H_2O and O_2 on all possible active sites of pristine and doped surfaces, which completes the calculations for the whole range of intermediates. From the adsorption energy values, it is evident that both H_2O and O_2 are chemisorbed on the pristine $CuCo_2S_4$ surface. Upon doping, the binding energies change significantly, with ΔG values closer to the thermoneutral condition. This suggests that initial intermediates (i.e. H_2O in the case of the OER and O_2 in the case of the ORR) neither bind too strongly nor too weakly on the doped $CuCoFeS_4$ surface, thereby making it a better catalyst for facilitating the OER and ORR processes. The optimized geometries of H_2O and O_2 adsorption on pristine and doped surfaces are depicted in Fig. S14–S17.

In addition to the free energy profiles for overpotential calculations, we also investigated the band structure and atom-projected density of states (DOS), which show the metallic nature of both the pristine and doped surfaces. It is anticipated

Table 2 Gibbs free energy values for all the active sites in pristine and doped $CuCo_2S_4$ in the ORR pathway

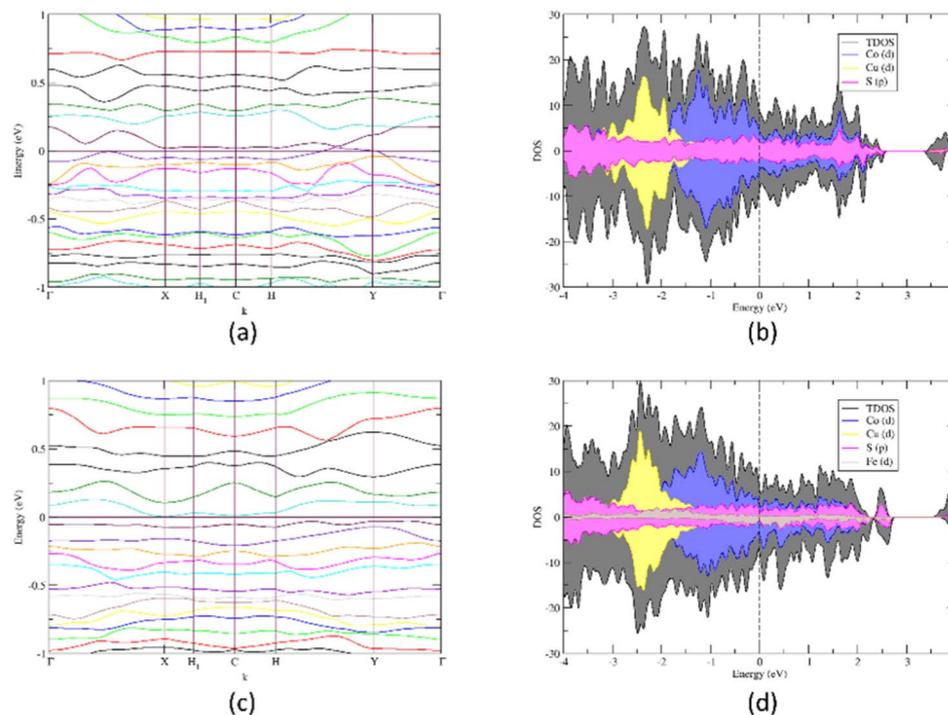| Surface(ORR)	Active site*	ΔG_1 (eV)	ΔG_2 (eV)	ΔG_3 (eV)	ΔG_4 (eV)	η_{ORR} (V)
$CuCo_2S_4$ (CCS)	Co	−1.84	−2.19	−0.95	0.08	1.31
	Cu	−0.93	−3.19	0.51	−1.32	1.74
$CuCoFeS_4$ ($Fe_xCuCo_2S_4$)	Co	−1.36	−1.72	−1.42	−0.42	0.81
	Cu	−0.56	−2.98	−0.19	−1.19	1.04
	Fe	−2.39	−2.1	−0.53	0.11	1.34

Fig. 13 Band structures and density of states for (a), (b) pristine and (c), (d) doped surfaces, respectively.

that the metallic surface acts as the source of free electrons for accelerating the catalytic process. The band structures and density of states plots are depicted in Fig. 13.

The atom-projected density of states shows a major contribution of Co-d orbitals near the Fermi level in the valence band of $CuCo_2S_4$, which acts as a potential source of electrons and thus plays a crucial role in the overall OER and ORR process. The doped surface also shows a similar behaviour. This is also reflected in the free energy profile, which shows that among all considered active sites, Co acts as the best possible site with the lowest overpotential for the OER and ORR on the pristine and doped surfaces.

These results suggest that the Fe doping is beneficial for enhancing both the OER and ORR catalytic performance, and thus, Fe-doped materials can be used as alternative cathode materials for rechargeable Zn–air batteries. Detailed XRD analysis indicates the existence of an optimum dopant concentration, beyond which new phase formation begins. Rietveld refinement confirms trace amounts of Cu_2S in all samples, with pristine $CuCo_2S_4$ exhibiting the highest content. Upon Fe incorporation, the Cu_2S phase decreases, correlating with enhanced OER and ORR performance. Both electrochemical measurements reveal that Fe doping in CCS must be carefully optimized, as excess Fe (>125 ppb) induces the formation of catalytically inferior FeS. Converging evidence from XRD, Raman spectroscopy, and XPS suggests that excessive FeS formation adversely affects oxygen reduction due to the reduction of catalytically active sites in the thiospinel. Microstructural characterization, electrochemical studies, and DFT calculations consistently identify $Fe_{0.03}CCS$ as the most effective catalyst. Detailed electrochemical analysis further confirms that

new phase formation degrades catalytic activity. The pristine $CuCo_2S_4$ catalyst exhibits bifunctional performance, achieving a half-wave potential of 0.76 V $vs.$ RHE for the ORR and an OER overpotential of 370 mV at 10 mA cm^{-2} ($\Delta E = 0.84$ V), resulting in a peak power density of 52 mW cm^{-2} and a specific capacity of 748.8 mA h g_{Zn}^{-1} in Zn–air batteries. Fe incorporation enhances these metrics, yielding a half-wave potential of 0.80 V and an OER overpotential of 330 mV ($\Delta E = 0.76$ V), corresponding to an impressive power density of 82 mW cm^{-2} and a specific capacity of 803.4 mA h g_{Zn}^{-1}. DFT calculations corroborate these findings, revealing that the initial intermediates (H_2O for the OER and O_2 for the ORR) bind neither too strongly nor too weakly on the Fe-doped $CuCo_2S_4$ surface, thereby facilitating efficient bifunctional oxygen electrocatalysis.

Conclusions

In summary, we report a single-step hydrothermal approach for synthesizing an Fe-doped $CuCo_2S_4$ thiospinel. A series of Fe_x-$CuCo_2S_4$ is successfully synthesized and demonstrated as an oxygen bifunctional electrocatalyst for both aqueous and solid rechargeable zinc–air batteries. The extensive experimental and theoretical investigations strongly suggest that Fe doping has a significant effect on oxygen electrocatalysis. The impact of Fe doping on the OH site effectively tunes the e_g occupancy of Co and therefore improves oxygen electrocatalysis. The Fe doping in the $CuCo_2S_4$ crystal increases the active site concentration ($C_{dl} \sim 28.84$ mF) as compared to pure $CuCo_2S_4$, which has a C_{dl} of 6.2 mF. Galvanostatic charge–discharge shows excellent stability for 75 hours with more than 200 cycles. Moreover, the

2232 | *J. Mater. Chem. A*, 2026, **14**, 2218–2234

This journal is © The Royal Society of Chemistry 2026

solid-state battery composed of $Fe_{0.03}CCS$ shows good stability for 25 hours with a specific capacity of 541 mA h g_{Zn}^{-1}. The demonstrated solid-state battery can glow an LED, showing the real-life application of our optimized catalyst. The demonstrated zinc–air battery with $Fe_{0.03}CCS$ as an air cathode shows excellent activity and higher stability. The Fe insertion into the thiospinel structure increases the catalytically active sites, which enhances the oxygen bifunctional behavior, making it a potential catalyst for advanced zinc–air battery applications. The outstanding durability and flexibility of the developed ZAB hold potential for portable and wearable electronic applications. The robust performance under repeated bending and continuous cycling indicates that the developed catalyst and electrode design are highly suitable for next-generation flexible energy devices.

Conflicts of interest

The authors share no conflicts of interests.

Data availability

The additional data supporting this article have been included as part of the supplementary information (SI). Supplementary information is available. See DOI: https://doi.org/10.1039/d5ta07350b.

Acknowledgements

References

1 Y. Liu, L. Zhou, S. Liu, S. Li, J. Zhou, X. Li, X. Chen, K. Sun, B. Li and J. Jiang, Fe, N-Inducing Interfacial Electron Redistribution in NiCo Spinel on Biomass-Derived Carbon for Bi-Functional Oxygen Conversion, *Angew. Chem.*, 2024, **136**(16), e202319983.

2 S. Kumar, R. Kumar, N. Goyal, S. K. Parida, A. Anshu, A. Yadav, F. Yan and B. Sahoo, Carbon nanostructures embedded with bimetallic CoRu alloy nanoparticles as oxygen reduction electrode for zinc–air batteries, *J. Mater. Chem. A*, 2025, **13**(14), 9992–10005.

3 Z. Li, S. Ji, C. Xu, L. Leng, H. Liu, J. H. Horton, L. Du, J. Gao, C. He and X. Qi, Engineering the electronic structure of single-atom iron sites with boosted oxygen bifunctional activity for zinc–air batteries, *Adv. Mater.*, 2023, **35**(9), 2209644.

4 J. Fu, Z. P. Cano, M. G. Park, A. Yu, M. Fowler and Z. Chen, Electrically rechargeable zinc–air batteries: progress, challenges, and perspectives, *Adv. Mater.*, 2017, **29**(7), 1604685.

5 J. Qian, X. Liu, C. Zhong, G. Xu, H. Li, W. Zhou, B. You, F. Wang, D. Gao and D. Chao, Enhanced stability and narrowed D-band gap of Ce-doped Co3O4 for rechargeable aqueous Zn-air battery, *Adv. Funct. Mater.*, 2023, **33**(9), 2212021.

6 H. Huang, Q. Liang, H. Guo, Z. Wang, G. Yan, F. Wu and J. Wang, Spray pyrolysis regulated FeCo alloy anchoring on nitrogen–doped carbon hollow spheres boost the performance of zinc–air batteries, *Small*, 2024, **20**(23), 2310318.

7 L. Chen, L. L. Cui, Z. Wang, X. He, W. Zhang and T. Asefa, Co8FeS8/N, S-doped carbons derived from Fe-Co/S-bridged polyphthalocyanine: efficient dual-function air-electrode catalysts for rechargeable Zn-air batteries, *ACS Sustain. Chem. Eng.*, 2020, **8**(35), 13147–13158.

8 T. Hu, Z. Jiang, Z. Fu and Z.-J. Jiang, A NiFe/NiSe 2 heterojunction bifunctional catalyst rich in oxygen vacancies introduced using dielectric barrier discharge plasma for liquid and flexible all-solid-state rechargeable Zn–air batteries, *J. Mater. Chem. A*, 2022, **10**(16), 8739–8750.

9 X. Chen, Z. Zhou, H. E. Karahan, Q. Shao, L. Wei and Y. Chen, Recent advances in materials and design of electrochemically rechargeable zinc–air batteries, *Small*, 2018, **14**(44), 1801929.

10 Y. Zhang, J. Wang, M. Alfred, P. Lv, F. Huang, Y. Cai, H. Qiao and Q. Wei, Recent advances of micro-nanofiber materials for rechargeable zinc-air batteries, *Energy Storage Mater.*, 2022, **51**, 181–211.

11 X. Zhu, C. Hu, R. Amal, L. Dai and X. Lu, Heteroatom-doped carbon catalysts for zinc–air batteries: progress, mechanism, and opportunities, *Energy Environ. Sci.*, 2020, **13**(12), 4536–4563.

12 T. Yu, Y. Zhang, Y. Hu, K. Hu, X. Lin, G. Xie, X. Liu, K. M. Reddy, Y. Ito and H.-J. Qiu, Twelve-component free-standing nanoporous high-entropy alloys for multifunctional electrocatalysis, *ACS Mater. Lett.*, 2021, **4**(1), 181–189.

13 N. Deng, Y. Wang, Q. Zeng, Y. Feng, G. Wang, H. Chi, W. Kang and B. Cheng, Facile construction of hierarchically porous carbon nanofibers modified by an FeCu/FeF 3 heterojunction for oxygen electrocatalysis in liquid and flexible Zn–air batteries, *J. Mater. Chem. A*, 2025, **13**(2), 1485–1498.

14 A. Singh, R. Sharma, A. Gautam, B. Kumar, S. Mittal and A. Halder, Chemistry in rechargeable zinc-air battery: a mechanistic overview, *Catal. Today*, 2025, **445**, 115108.

15 M. Chen and J. Guan, Structural Regulation Strategies of Atomic Cobalt Catalysts for Oxygen Electrocatalysis, *Adv. Funct. Mater.*, 2025, 2423552.

16 A. Kundu, T. Kuila, N. C. Murmu, P. Samanta and S. Das, Metal–organic framework-derived advanced oxygen electrocatalysts as air-cathodes for Zn–air batteries: recent

This journal is © The Royal Society of Chemistry 2026

J. Mater. Chem. A, 2026, **14**, 2218–2234 | **2233**

trends and future perspectives, *Mater. Horiz.*, 2023, **10**(3), 745–787.

17 J. Zhang, H. B. Tao, M. Kuang, H. B. Yang, W. Cai, Q. Yan, Q. Mao and B. Liu, Advances in thermodynamic-kinetic model for analyzing the oxygen evolution reaction, *ACS Catal.*, 2020, **10**(15), 8597–8610.

18 G. Nazir, A. Rehman, J.-H. Lee, C.-H. Kim, J. Gautam, K. Heo, S. Hussain, M. Ikram, A. A. AlObaid and S.-Y. Lee, A review of rechargeable zinc–air batteries: Recent progress and future perspectives, *Nano-Micro Lett.*, 2024, **16**(1), 138.

19 S. Ren, X. Duan, S. Liang, M. Zhang and H. Zheng, Bifunctional electrocatalysts for Zn–air batteries: recent developments and future perspectives, *J. Mater. Chem. A*, 2020, **8**(13), 6144–6182.

20 S. Lee, J. Choi, M. Kim, J. Park, M. Park and J. Cho, Material design and surface chemistry for advanced rechargeable zinc–air batteries, *Chem. Sci.*, 2022, **13**(21), 6159–6180.

21 J. Chang, G. Wang and Y. Yang, Recent advances in electrode design for rechargeable zinc–air batteries, *Small Sci.*, 2021, **1**(10), 2100044.

22 X. Liu, Y. Zhu, C. Du, J. Tian, L. Yang, X. Yao, Z. Wang, X. Ma, J. Hou and C. Cao, Cationic Co-doping in copper sulfide nanosheet cathodes for efficient magnesium storage, *Chem. Eng. J.*, 2023, **463**, 142433.

23 Y. Zhang, L. Tao, C. Xie, D. Wang, Y. Zou, R. Chen, Y. Wang, C. Jia and S. Wang, Defect engineering on electrode materials for rechargeable batteries, *Adv. Mater.*, 2020, **32**(7), 1905923.

24 Y. Qin, G. Lu, F. Yang, C. Xu, S. Jiang, Y. Wang, Y. Tang and P. Wang, Heteroatom-doped transition metal hydroxides in energy storage and conversion: a review, *Mater. Adv.*, 2023, **4**(5), 1226–1248.

25 M. Chauhan, K. P. Reddy, C. S. Gopinath and S. Deka, Copper cobalt sulfide nanosheets realizing a promising electrocatalytic oxygen evolution reaction, *ACS Catal.*, 2017, **7**(9), 5871–5879.

26 L. Yan, B. Xie, C. Yang, Y. Wang, J. Ning, Y. Zhong and Y. Hu, Engineering self-supported hydrophobic–aerophilic air cathode with CoS/Fe3S4 nanoparticles embedded in S, N Co-doped carbon plate arrays for long-life rechargeable Zn–air batteries, *Adv. Energy Mater.*, 2023, **13**(10), 2204245.

27 G. Fu, J. Wang, Y. Chen, Y. Liu, Y. Tang, J. B. Goodenough and J. M. Lee, Exploring indium-based ternary thiospinel as conceivable high-potential air-cathode for rechargeable Zn–Air batteries, *Adv. Energy Mater.*, 2018, **8**(31), 1802263.

28 G. Fu, Y. Wang, Y. Tang, K. Zhou, J. B. Goodenough and J.-M. Lee, Superior oxygen electrocatalysis on nickel indium thiospinels for rechargeable Zn–air batteries, *ACS Mater. Lett.*, 2019, **1**(1), 123–131.

29 L. Nie, H. Wang, Y. Chai, S. Liu and R. Yuan, In situ formation of flower-like $CuCo_2S_4$ nanosheets/graphene composites with enhanced lithium storage properties, *RSC Adv.*, 2016, **6**, 38321–38327.

30 S. Liu, B. Zhang, Y. Cao, H. Wang, Y. Zhang, S. Zhang, Y. Li, H. Gong, S. Liu and Z. Yang, Understanding the effect of nickel doping in cobalt spinel oxides on regulating spin state to promote the performance of the oxygen reduction reaction and zinc–air batteries, *ACS Energy Lett.*, 2022, **8**(1), 159–168.

31 J. K. Nørskov, T. Bligaard, A. Logadottir, J. Kitchin, J. G. Chen, S. Pandelov and U. Stimming, Trends in the exchange current for hydrogen evolution, *J. Electrochem. Soc.*, 2005, **152**(3), J23.